Monthly Notices
of the
ROYAL ASTRONOMICAL SOCIETY

MNRAS **461,** 111–125 (2016)
Advance Access publication 2016 June 15

doi:10.1093/mnras/stw1307

Positive or negative? The impact of X-ray feedback on the formation of direct collapse black hole seeds

John A. Regan,[1]★ Peter H. Johansson[2] and John H. Wise[3]

[1]*Institute for Computational Cosmology, Durham University, South Road, Durham DH1 3LE, UK*
[2]*Department of Physics, University of Helsinki, Gustaf Hällströmin katu 2a, FI-00014 Helsinki, Finland*
[3]*Center for Relativistic Astrophysics, Georgia Institute of Technology, 837 State Street, Atlanta, GA 30332, USA*

Accepted 2016 May 27. Received 2016 May 27; in original form 2016 March 21

ABSTRACT

A nearby source of Lyman–Werner (LW) photons is thought to be a central component in dissociating H_2 and allowing for the formation of a direct collapse black hole seed. Nearby sources are also expected to produce copious amounts of hydrogen ionizing photons and X-ray photons. We study here the feedback effects of the X-ray photons by including a spectrum due to high-mass X-ray binaries on top of a galaxy with a stellar spectrum. We explicitly trace photon packages emerging from the nearby source and track the radiative and chemical effects of the multifrequency source ($E_{\rm photon} = 0.76\,{\rm eV} \rightarrow 7500\,{\rm eV}$). We find that X-rays have a strongly negative feedback effect, compared to a stellar only source, when the radiative source is placed at a separation greater than $\gtrsim$1 kpc. The X-rays heat the low and medium density gas in the envelope surrounding the collapsing halo suppressing the mass inflow. The result is a smaller enclosed mass compared to the stellar only case. However, for separations of $\lesssim$1 kpc, the feedback effects of the X-rays becomes somewhat neutral. The enhanced LW intensity at close separations dissociates more H_2 and this gas is heated due to stellar photons alone, the addition of X-rays is then not significant. This distance dependence of X-ray feedback suggests that a Goldilocks zone exists close to a forming galaxy where X-ray photons have a much smaller negative feedback effect and ideal conditions exist for creating massive black hole seeds.

Key words: methods: numerical – stars: Population III – cosmology: theory.

1 INTRODUCTION

The discovery of a large number of supermassive black holes (SMBHs) in the early Universe presents a challenge to our understanding of the formation of compact objects in the first billion years. How could such massive objects form and grow to such huge masses so quickly? The most distant SMBH that has been observed has a redshift of $z = 7.085$ and a mass of $\sim 2 \times 10^9$ M$_\odot$ (Mortlock et al. 2011) while the most massive SMBH observed in the early Universe has a mass of $\sim 1.2 \times 10^{10}$ M$_\odot$ at a redshift of $z = 6.30$ (Wu et al. 2015). If, as expected, a massive star must be the progenitor for these SMBHs then the stellar remnant must grow at enormous rates (most likely at or above the Eddington rate for its entire growth phase) to reach the huge black hole masses observed. Simulations of the formation and evolution of the first stars show that the characteristic mass of the first metal-free stars is expected to be around 40 M$_\odot$ (Stacy, Greif & Bromm 2010; Clark et al. 2011; Greif et al. 2011; Bromm 2013; Hirano et al. 2014; Safranek-Shrader et al. 2016; Valiante et al. 2016) leading to remnant black hole masses which must grow by up to eight orders of magnitude by $z \sim 7$. Further exacerbating the situation is that these Population III (Pop III) stars are expected to form in low mass haloes (see e.g. Bromm & Yoshida 2011). The resultant supernova are then expected to expel the gas from the halo further hampering the growth (Johnson & Bromm 2007; Alvarez, Wise & Abel 2009; Milosavljević, Couch & Bromm 2009; Hosokawa et al. 2011) of the black hole and almost certainly restricting the black hole growth to values much less than the Eddington rate. All of these obstacles combine to make Pop III stars rather unattractive progenitors for the SMBHs observed at early times.

If instead we form supermassive stars (SMS), with initial masses of $\gtrsim 10^3$ M$_\odot$, in more massive haloes, in the early Universe we can conveniently side-step the growth requirements. The initial star grows to supermassive scales via mass accretion (e.g. Hosokawa et al. 2013) reaching a mass of a few times 10^5 M$_\odot$ before undergoing a general relativistic instability (e.g. Shibata, Uchida & Sekiguchi 2016). SMS are expected to directly collapse into black holes with masses close to that of the progenitor (see e.g. Chandrasekhar 1964). As a result the black hole gets a head start

★E-mail: john.a.regan@durham.ac.uk

compared to a comparatively small Pop III star. Direct collapse black holes (DCBHs) then offer a promising mechanism to explain the existence of quasars at redshifts greater than six. Numerous analytical, semi-analytical and numerical studies have been undertaken in recent years to study in great detail the direct collapse mechanism (Bromm & Loeb 2003; Wise, Turk & Abel 2008; Regan & Haehnelt 2009b,a; Tseliakhovich & Hirata 2010; Inayoshi & Omukai 2012; Agarwal et al. 2013; Latif et al. 2013; Agarwal et al. 2014; Regan, Johansson & Haehnelt 2014a; Regan, Johansson & Wise 2014b; Tanaka & Li 2014; Inayoshi, Visbal & Kashiyama 2015; Mayer et al. 2015). In order to form an SMS we need to disrupt the usual mechanisms that lead to the formation of Pop III stars. H_2 is the dominant coolant in the early Universe, if this cooling channel is blocked then the gas will remain at the atomic cooling threshold of $T \sim 8000$ K assuming it is also metal free (for atomic cooling haloes with $T_{\rm vir} \sim 10^4$ K). Eliminating H_2 can be achieved either through photodissociation or collisional dissociation.

Collisional dissociation of H_2 ($H_2 + H \rightarrow 3\ H$) is effective for gas of a primordial composition and high temperature satisfying the criteria of the 'zone of no-return' (Visbal, Haiman & Bryan 2014a). Inayoshi & Omukai (2012) suggested that cold accretion shocks may provide a pathway to collisionally dissociate H_2 during gravitational collapse. However, Fernandez et al. (2014) demonstrated, through numerical simulations, that in the absence of a photodissociating background this method is difficult to achieve in practice as the collisional processes tend to operate at the virial radius and not in the centre of the halo.

Photodissociation of H_2 has been studied by several authors as a viable means of disrupting H_2 cooling at high redshift where metal cooling is unavailable (Omukai 2001; Oh & Haiman 2002; Bromm & Loeb 2003; Shang, Bryan & Haiman 2010; Latif et al. 2014a,b, 2015). In this case radiation in the Lyman–Werner (LW) band with energies between 11.2 and 13.6 eV is able to dissociate H_2 via the two-step Solomon process (Field, Somerville & Dressler 1966; Stecher & Williams 1967).

$$H_2 + \gamma \rightarrow H_2^* \quad (1)$$

$$H_2^* \rightarrow H + H + \gamma \quad (2)$$

In order for a halo to receive a large H_2 dissociating flux it must be near a luminous star-forming galaxy which will irradiate the protogalactic cloud and which may augment an already existing background flux. However, star-forming galaxies will also produce copious amount of hydrogen ionizing radiation (hereafter ionizing radiation) which will photoionize and heat the gas as well as destroying H_2. While the mean free path of ionizing radiation will be much shorter than LW radiation, for haloes which are sufficiently close the H II region created by the ionizing flux will be important. Further study has been dedicated to the study of X-ray backgrounds which are expected to become relevant as the number density of X-ray sources increases. Recently, Hummel et al. (2015) have investigated the impact of a cosmic X-ray background on Pop III formation while both Inayoshi & Omukai (2011); Inayoshi & Tanaka (2015) and Latif et al. (2015) have investigated the impact of X-ray backgrounds on the DCBH paradigm. As these works are closely related to the study here we will reflect on all of these studies in Sections 3.3 and 4.

In (Regan, Johansson & Wise 2016, hereafter R16) we investigated the impact of radiation from a nearby source with photon energies up to 60 eV (i.e. stellar only model). We found that for very closely separated haloes ($R \lesssim 0.5$ kpc) the proto-halo was photoevaporated while for haloes that are too distant ($R > 4.0$ kpc) the impact of the LW flux was insignificant. We determined that for haloes separated by approximately 1 kpc, the flux received from a single nearby realistic galaxy resulted in the formation of a large core[1] mass of close to $M_{\rm core} \sim 10^4 M_\odot$ with a core temperature of $T \sim 1000$ K surrounded by a large reservoir of warm gas ($T_{\rm vir} \sim 10^4$ K). Such an environment should represent an ideal location for forming an SMS.

In this paper we expand on our previous study by also considering the impact of both soft and hard X-rays. Nearby galaxies as well as supplying a strong source of LW and ionizing photons should also produce a supply of X-ray photons through the formation of high-mass X-ray binaries (HMXBs) as massive stars reach the end of the lifetimes. The goal of this paper is then to investigate this important scenario and to determine whether X-rays have a negative or positive effect on the direct collapse scenario when a collapsing halo is irradiated by an anisotropic source. As in R16 our intention is therefore not to investigate the numerical value of '$J_{\rm crit}$'[2] in this instance but rather taking the results of the 'Renaissance' Simulation suite (see Section 2.2) to investigate the impact of a realistic source on a nearby galaxy. Our results, similar to R16, will in fact show that achieving complete H_2 dissociation through irradiation from a single close-by neighbour is very unlikely (see R16 for a comprehensive discussion on this topic) and will require (if full H_2 dissociation is indeed ever required) more than one nearby source. In this sense we do not simulate the classical DCBH formation case and rather we instead focus on simulating realistic environments from first principles without invoking idealized conditions (e.g. ultra-strong radiation fields) conductive to DCBH formation.

The paper is laid out as follows: in Section 2 we describe the model setup and the numerical approach used, the chemical model and radiation prescription employed; in Section 3 we describe the results of our numerical simulations; in Section 4 we discuss the importance of the results and in Section 5 we present our conclusions. Throughout this paper we assume a standard ΛCDM cosmology with the following parameters (Planck Collaboration XVI 2014, based on the latest Planck data), $\Omega_{\Lambda,0} = 0.6817$, $\Omega_{\rm m,0} = 0.3183$, $\Omega_{\rm b,0} = 0.0463$, $\sigma_8 = 0.8347$ and $h = 0.6704$. We further assume a spectral index for the primordial density fluctuations of $n = 0.9616$.

2 MODEL SETUP

The numerical model used in this study is very similar to the model used in R16. The significant difference is that in this work the effect of X-ray radiation is included in the model. Furthermore, compared to R16 an additional realization is used. We refer to the first halo as Halo A (this is the same halo as used in R16) and the second halo as Halo B.

2.1 Numerical framework

We ran our simulations using the publicly available adaptive mesh refinement (AMR) code ENZO(Bryan et al. 2014).[3] In particular we use version 3.0[4] which is the bleeding edge version of the code

[1] The core of the halo is defined at the point where the baryonic mass exceeds the dark matter mass. This fluctuates between approximately 1 pc and 5 pc across the simulations. We therefore choose 1 pc to define the radius of the core of the halo in all cases for consistency.

[2] $J_{\rm crit}$ is taken to be value of the background radiation intensity required to fully dissociate H_2 from a target halo.

[3] http://enzo-project.org/

[4] Changeset: 7f49adb4c9b4

incorporating a range of new features. We created a fork off the 3.0 mainline and included improved support for radiative transfer based on the Moray implementation of Wise & Abel (2011) and chemical modelling using the `Grackle` library. For a more in depth discussion of the ray tracing elements and of the modifications to the chemical network see R16.

All simulations are run within a box of 2 h^{-1} Mpc (comoving), the root grid size is 256^3 and we employ three levels of nested grids. The grid nesting and initial conditions are created using the MUSIC software package (Hahn & Abel 2011). Within the most refined region (i.e. level 3) the dark matter particle mass is ∼103 $M_\odot$. In order to increase further the dark matter resolution of our simulations we split the dark matter particles according to the prescription of Kitsionas & Whitworth (2002) and as described in Regan, Johansson & Wise (2015). We split particles centred on the position of the final collapse as found from lower resolution simulations within a region with a comoving side length of 43.75 h^{-1} kpc. Each particle is split into 13 daughter particles resulting in a final dark matter particle mass of ~ 8 $M_\odot$ in the high resolution region. The particle splitting is performed at a redshift of $z = 40$ well before the collapse of the target halo. Convergence testing to study the impact of lower dark matter particle masses on the physical results was conducted as discussed in R16. All of the simulations are started from a redshift of $z = 100$.

The baryon resolution is set by the size of the grid cells, in the highest resolution region this corresponds to approximately 0.48 h^{-1} kpc comoving (before adaptive refinement). The maximum refinement level for all of the simulations was set to 16 leading to a maximum spatial resolution of $\Delta x \sim 5 \times 10^{-3}$ pc at a redshift of $z = 25$. The refinement criteria used in this work were based on three physical measurements. (1) The dark matter particle over-density, (2) The baryon over-density and (3) the Jeans length. The first two criteria introduce additional meshes when the over-density ($\frac{\Delta\rho}{\rho_{\rm mean}}$) of a grid cell with respect to the mean density exceeds 8.0 for baryons and/or DM. Furthermore, we set the *MinimumMassForRefinementExponent* parameter to −0.1 making the simulation super-Lagrangian and therefore reducing the threshold for refinement as higher densities are reached. For the final criteria we resolve the local Jeans length by at least 16 cells in these runs. All simulations are run until they reach the maximum refinement level at which point the simulation is terminated.

2.2 Radiation source

As in R16 we use a radiation source to model the impact of a nearby galaxy on a collapsing halo. The radiation source is a point particle. It is massless and is fixed in comoving space. The physical distance between the source and the collapsing halo therefore inevitably increases due to the expansion of the Universe as a function of decreasing redshift. The source of radiation is placed at a distance of between 1 kpc and 4 kpc, depending on the given model being tested, from the point of maximum density at a redshift of $z = 40$. In each case, we use a luminosity of 1.2×10^{52} photons per second (above the H^- photodetachment energy of 0.76 eV) that originates from a galaxy with a stellar mass of 10^3 $M_\odot$ at $z = 40$. The galaxy has a specific star formation rate (SFR) of sSFR = 40 Gyr^{-1} resulting in a stellar mass of 10^5 $M_\odot$ at $z = 20$. The stellar mass at $z = 20$ and the specific SFR are consistent with the largest galaxies prior to reionization in the Renaissance Simulations of Chen et al. (2014). We then calculate its spectrum with the Bruzual & Charlot (2003) models with a metallicity of 10^{-2} $Z_\odot$ and compute the photon luminosity from it. Furthermore, for the models which include X-rays we include the contribution from six HMXB sources (see Section 2.5). The spectrum does not include emission from the nebular component and is solely due to stellar and X-ray emission from individual sources.

2.3 Radiation fields

In total three different radiation fields were used in this study. The three fields are detailed in Table 1. The first field has contributions from a stellar source only. The last two fields are broken into two parts both with contributions from stellar and X-ray components. The second field in the table is composed of radiation from a stellar component and a soft X-ray component, with energies up to 380 eV. The third field in the table extends the X-ray contribution into the hard X-ray regime with contributions of energies up to 7570 eV.

The optimal energy bins with which to model our spectra are computed using the SEDOP code developed by Mirocha et al. (2012). The SEDOP code determines the optimum energy and intensity for a given number of energy bins needed to accurately model radiation with energy above the ionization threshold of hydrogen. The energy bins below the ionization threshold are set to capture the peak of the photodetachment of H^- at 0.76 eV, photoionizations of H_2^+ at 8.0 eV and photoionizations of H_2 at 12.8 eV.

The shape of the stellar spectrum used in this study (see Fig. 1) is identical to the one used in R16. In particular the left-hand panel of Fig. 1 includes only the spectrum due to a stellar component and is described in Section 2.2. The right-hand panel shows the extra contribution to the spectrum when X-rays are included. For including the X-ray contribution to the spectrum we assume that the X-ray luminosity is evenly split between a multicolour disc component (Mitsuda et al. 1984) formed from the accretion disc feeding the black hole and a non-thermal component (power law) formed from the Comptonization of electrons, originating in the disc, in the hot corona surrounding the black hole. This model is similar to that used by numerous models of black hole spectra in the literature (Zdziarski et al. 2001; Kuhlen & Madau 2005; Done, Gierliński & Kubota 2007). We assume that there are six HMXB sources, as was typically observed in the Renaissance simulations (Xu, Wise & Norman 2013), active within the galaxy, we take a mass of 40 $M_\odot$ for each of the black holes and finally we assume a radiative efficiency of 0.1 times Eddington. The photon fraction (i.e. SED component) in each energy bin is then taken from the spectrum.

Finally, we break the X-ray spectra into two further models. For the first model we take into account the contribution of a stellar component and a soft X-ray component and impose a cut-off at ∼380 eV, we refer to this model as the soft X-ray model. For the second X-ray model we take both the soft and hard components of the spectrum into account as well as the stellar component and allow the X-rays to reach energies up to ∼ 7500 eV, we refer to this model as the hard X-ray model. Each of three models includes a stellar component with energies up to ∼ 60 eV.

2.4 Modelling absorption due to gas in the interstellar medium

We also model the impact of interstellar absorption of ultraviolet photons (with energies greater than 13.6 eV) in our model. The impact of this modelling can be seen in the sharp drop in photon numbers above 13.6 eV. The model convolves the spectral energies

Table 1. Radiation SED.

Spectrum	Energy bins (eV)	Photon fraction (PF)
Stellar	0.76, 8.0, 12.8, 14.79, 20.46, 27.62, 60.0	0.4130, 0.3170, 0.1080, 1.32e-07, 2.23e-04, 3.49e-03, 2.26e-02
Stellar + Soft X-rays	0.76, 8.0, 12.8, 14.54, 21.87, 119.67, 380.12	0.4130, 0.3170, 0.1080, 6.65e-08, 1.22e-04, 1.78e-02, 9.53e-03
Stellar + Hard X-rays	0.76, 8.0, 12.8, 17.84, 25.06, 52.93, 69.47, 137.11, 252.82, 750.29, 7570.53	0.4130, 0.3170, 0.1080, 6.21e-06, 4.42e-04, 5.05e-03, 8.29e-03, 6.923-03, 9.59e-03, 5.77e-03, 7.05e-03

Notes. The energy bins and the fractional number of photons are given for the stellar spectrum and the stellar + X-ray spectrum for the cases of both soft (<1 keV) and hard X-rays (>1 keV). The photon fractions are given for all three cases. In each case the photon energies and fractions are identical for energies below the ionization threshold of hydrogen. For energies above the ionization threshold the sampling energies and sampling fractions are taken from the SEDOP code developed by Mirocha et al. (2012) which optimizes the number and position of the energy bins required.

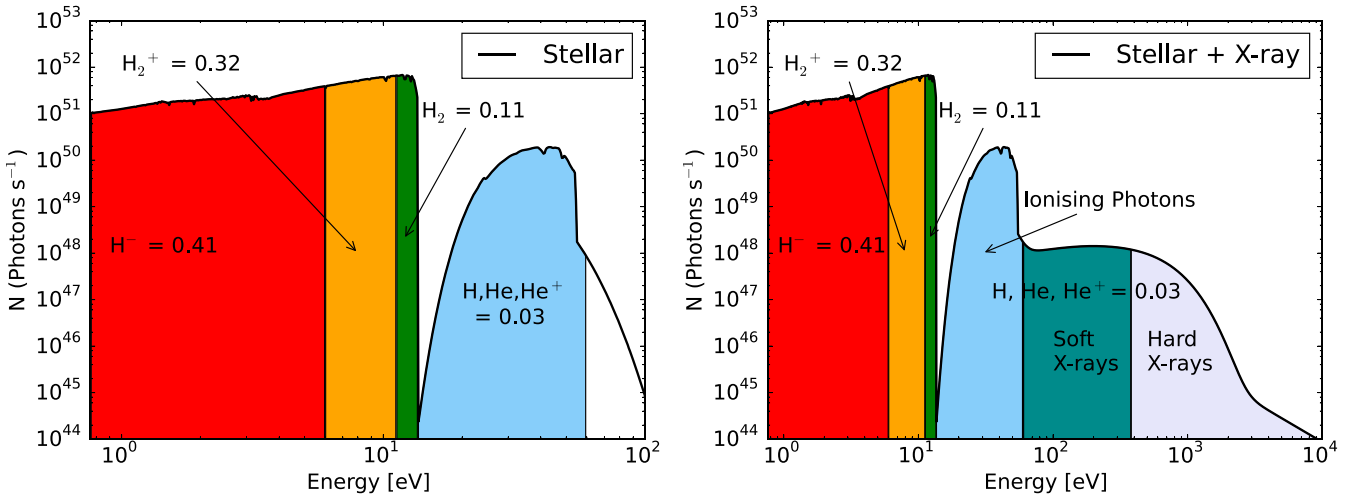

Figure 1. The left-hand panel shows the luminosity from a stellar spectrum consistent with the Renaissance Simulation of Chen et al. (2014). The total stellar mass giving rise to this spectrum is 10^5 $M_\odot$ at $z = 20$. We have employed an extinction factor for photons with energy greater than 13.6 eV and a cutoff for photons greater than 60 eV. In the right-hand panel we show the same plot with the inclusion of X-rays evenly split between a non-thermal source and a multicolour disc component. The fraction of photons in each energy band is indicated. In both panels the number of photons in each bin is almost the same as the vast majority of the photons have energies less than the ionization threshold for hydrogen. The main difference therefore is that the X-rays are in addition sampled in the right-hand plot. The contribution of X-ray photons to the total number photons is relatively small.

of our spectra with a simple modelling of the optical depth to ionizing radiation as follows:

$$\mathrm{PF_{ext}(E)} = \mathrm{PF(E)} \times \exp(-\sigma(\mathrm{E}) \times \mathrm{N(H\,I)_{avg}}) \quad (3)$$

where PF(E) is the photon fraction at the energy, E, $\mathrm{PF_{ext}(E)}$ is the photon fraction when the extinction is accounted for, σ(E) is the cross-section of hydrogen at that energy and $\mathrm{N(H\,I)_{avg}}$ is the column density of hydrogen averaged over the source galaxy. For our model we choose an average value of $\mathrm{N(H\,I)_{avg}}$ of $2.5 \times 10^{18}\mathrm{cm}^{-2}$ consistent with the results from the simulations of Wise & Cen (2009). A full description of the physical motivations of this model along with the assumptions incorporated into the model is given in R16.

2.5 Modelling the contribution due to X-rays

The major difference between this work and that of R16 is the inclusion of an X-ray component. The ionization cross-sections of neutral hydrogen and helium drop off as $\sigma_H(\nu) \propto \nu^{-3}$ and $\sigma_{He}(\nu) \propto \nu^{-2}$, respectively as the photon energy increases. As a result X-ray photons have a much longer mean free path than ionizing photons with energies close to 13.6 eV. To model the X-ray photon effect on the gas we make use of the ray-tracing capabilities of ENZO (Abel & Wandelt 2002; Wise & Abel 2011). Within ENZO X-rays are defined as photons with energies greater than 100 eV. As a consequence and based on the results of SEDOP we have two X-ray energy bins with a soft X-ray spectrum and four energy bins with a hard X-ray spectrum. For each energy bin, including X-rays, 768 (12×4^3; Healpix level 3) rays are isotropically cast with the energy associated with that bin. Consequently, the number of photons per each initial ray is

$$P_{\mathrm{init}} = \frac{L_{\mathrm{gal}} \times \mathrm{PhotonFraction} \times \mathrm{d}t_{\mathrm{ph}}}{768 \times E_{\mathrm{ph}}} \quad (4)$$

where L_{gal} is the total bolometric luminosity of our galactic source (1.64×10^{41} erg s^{-1}), Photon Fraction is the fraction of the photons in a given energy bin (see Table 1 for values), $\mathrm{d}t_{\mathrm{ph}}$ is the photon timestep used and E_{ph} is the photon energy for that ray. Each ray is traced until most of its photons are absorbed (99.999 99 per cent) or the photon reaches the end of its region of influence, which we set as 10 per cent of the computational domain. As rays propagate through the computational domain they are split based on the HEALPix formalism.

As the X-ray photons propagate into the surrounding medium they interact with the gas in two ways: they (1) ionize the hydrogen

and helium and (2) they heat the gas.[5] Since X-ray photons have energies in excess of the double ionization threshold of helium the X-ray photons can photoionize H, He and He^+ with the respective photoionization rates:

$$k_{\rm ph,H} = \frac{P_{\rm in}(1-e^{-\tau_H})(E_{\rm ph}Y_{k,H}/E_{i,H})}{n_H(\Delta x)^3 {\rm d}t_{\rm ph}}$$
$$k_{\rm ph,He} = \frac{P_{\rm in}(1-e^{-\tau_{\rm He}})(E_{\rm ph}Y_{k,{\rm He}}/E_{i,{\rm He}})}{n_{\rm He}(\Delta x)^3 {\rm d}t_{\rm ph}}$$
$$k_{\rm ph,He^+} = \frac{P_{\rm in}(1-e^{-\tau_{\rm He^+}})}{n_{\rm He^+}(\Delta x)^3 {\rm d}t_{\rm ph}} \quad (5)$$

where $P_{\rm in}$ is the number of photons entering a cell, $\tau_H = n_H\sigma_H(E){\rm d}l$ is the optical depth in that cell, n_H is the hydrogen number density, $\sigma_H(E)$ is the energy dependent hydrogen photoionization cross-section (Verner et al. 1996), dl is the path length through that cell and E_i are the ionization thresholds for H, He and He^+ respectively. All of the above hydrogen subscripts apply equally to helium and ionized helium. The factors Y_k are the energy fractions used for the ionization when secondary ionizations are also considered (Shull & van Steenberg 1985). In the case of secondary ionizations the primary electron which is freed in the original ionization is free not only to heat the gas but also to cause further ionizations due to its large kinetic energy. The secondary ionization is then more effective than the primary ionization when considering X-ray ionizations of H and He. For He^+, however, the impact of secondary ionizations are not important (Shull & van Steenberg 1985).

Finally, photons also heat the gas through both excess energy heating and Compton heating. The excess energy above the ionization threshold for each ion, E_i, heats each of the ions according to

$$\Gamma_H = \frac{P_{\rm in}(1-e^{-\tau_H})E_{\rm ph}Y_\Gamma}{n_H(\Delta x^3){\rm d}t_{\rm ph}} \quad (6)$$

with the same equation applying equally to the helium ions, where Γ_H is the heat imposed on species H, Y_Γ is the fraction of energy deposited as heat when secondary ionizations are taken into account. The X-rays can also scatter off and heat an electron leading to an extra contribution of the form

$$\Gamma_C = \frac{P_{\rm in}(1-e^{-\tau_e})\Delta E(T_e)}{n_H(\Delta x)^3 {\rm d}t_{\rm ph}} \quad (7)$$

where $\tau_e = n_e\sigma_{\rm KN}{\rm d}l$ is the optical depth, n_e is the electron number density, $\sigma_{\rm KN}$ is the non-relativistic Klein–Nishina cross-section (Rybicki & Lightman 1979) and $\Delta E(T_e) = 4k_bT_e(E_{\rm ph}/m_ec^2)$ is the non-relativistically transferred energy to an electron at T_e (Ciotti & Ostriker 2001). It should also be noted that in this case the photon continues to propagate and is not absorbed. As a result the total heating rate is

$$\Gamma_{\rm Total} = n_H\Gamma_H + n_{\rm He}\Gamma_{\rm He} + n_{\rm He^+}\Gamma_{\rm He^+} + n_e\Gamma_C \quad (8)$$

A model similar to this was previously implemented and tested in ENZOby Kim et al. (2011) although in their case the energy of the X-rays was fixed at 2 keV and the context was the exploration of the feedback from black holes at a much lower redshift of $z \sim 3$.

[5] Both infrared photons and ionizing photons also heat the gas but to a much lesser extent (see Fig. 11).

2.6 Chemical network

We adopt here the 26 reaction network determined by Glover (2015a) as the most appropriate network for solving the chemical equations required by the direct collapse model in a gas of primordial composition with no metal pollution. The network consists of ten individual species: H, H^+, He, He^+, He^{++}, e^-, H_2, H_2^+, $H^-$and HeH^+. Additionally, we included a further seven reactions which accounts for the recombinations (4) and photoionizations (3) of H, He, and He^+ which occurs when the elements are photoionized due to photon energies greater than 13.6 eV, 25.4 eV and 54.4 eV, respectively.

To implement the chemical network we have extensively modified the open source code GRACKLE-2.1[6,7] (Bryan et al. 2014; Kim et al. 2014). GRACKLE-2.1self-consistently solves the 33 set reaction network including photoionizations. The network includes the most up-to-date rates as described in Glover & Jappsen (2007), Glover & Abel (2008), Glover & Savin (2009), Coppola et al. (2011), Coppola et al. (2012), Glover (2015a), Glover (2015b), Latif et al. (2015). The reaction network is described in full in R16. The gas is allowed to cool radiatively during the simulation and this is also accounted for using the GRACKLE-2.1module. Here the rates have again been updated to account for recent updates in the literature (Glover 2015a). The cooling mechanisms included in the model are collisional excitation cooling, collisional ionization cooling, recombination cooling, bremsstrahlung and Compton cooling off the CMB.

2.7 Realizations

In this study we compare two different realizations which we name Halo A and Halo B. Both haloes were previously determined in Regan et al. (2015) and created with the MUSIC code. Using exactly the same methods as employed in R16 we place a radiating source (i.e. a 'galaxy') close to a collapsing halo and investigate the effects of the realistic radiation field on the collapse of the halo and determine the viability of the direct collapse method. The idea that close-by neighbours are required for direct collapse has previously been studied analytically by Dijkstra et al. (2008), Dijkstra, Ferrara & Mesinger (2014) and more recently using synchronized halo pairs by Visbal, Haiman & Bryan (2014b). For each simulation we switch on the radiating source at a redshift of $z = 40$ and place the source at a distance of 1 kpc, 2 kpc or 4 kpc physical from the target halo (i.e. point of maximum density at that redshift). We do not investigate sources for which the separation is less than 1 kpc as we found in R16 that this results in complete photoevaporation of the halo. For each distance separation we also vary the spectrum of the radiating source. The spectrum is either a stellar only spectrum, a soft X-ray spectrum or a hard X-ray spectrum (see Fig. 1). However, in all cases the spectrum is *always* stellar for the first ∼20 Myr i.e. between a redshift of $z = 40$ and $z = 33$. At a redshift of $z = 33$ we either do nothing (stellar only case) or we update the spectrum to include soft X-rays (soft X-ray model) or we update the spectrum to include both soft and hard X-rays (hard X-ray model). The time between when the galaxy emits only stellar photons and when it begins to emit stellar plus X-ray photons is clearly uncertain. Our estimation of 20 Myr takes into account the typical time-scale of massive stellar evolution and the fact it takes time to build up a significant X-ray presence through binary evolution. In Table 2 we have outlined each

[6] https://grackle.readthedocs.org/
[7] Changeset: 88143fb25480

Table 2. Realizations and models.

Sim name	Init. dist. (kpc)	Spectrum	$z_{\rm coll}$	Final dist. (kpc)	$T_{\rm vir}$ (K)	M_{200} ($M_\odot$)	$M_{\rm core}$ ($M_\odot$)
1kpc_S_A	1.0	Stellar SED	25.25	1.9	6224	1.04×10^7	9476
2kpc_S_A	2.0	Stellar SED	28.67	2.9	4225	4.84×10^6	7269
4kpc_S_A	4.0	Stellar SED	29.97	5.4	3181	2.96×10^6	6117
1kpc_X_A	1.0	Stellar + XRay SED	25.13	1.9	6513	1.12×10^7	8475
2kpc_X_A	2.0	Stellar + XRay SED	29.06	2.9	3849	4.12×10^6	5903
4kpc_X_A	4.0	Stellar + XRay SED	31.06	5.2	2212	1.63×10^6	3092
1kpc_HX_A	1.0	Stellar + Hard XRay SED	24.54	2.0	8675	1.74×10^7	5174
2kpc_HX_A	2.0	Stellar + Hard XRay SED	29.48	2.8	3434	3.40×10^6	5692
4kpc_HX_A	4.0	Stellar + Hard XRay SED	31.08	5.2	2210	1.63×10^6	3040
1kpc_S_B	1.0	Stellar SED	21.41	1.4	9830	2.62×10^7	7587
2kpc_S_B	2.0	Stellar SED	28.44	2.5	4332	5.08×10^6	10 936
4kpc_S_B	4.0	Stellar SED	29.97	5.1	3253	3.06×10^6	6562
1kpc_X_B	1.0	Stellar + XRay SED	21.98	1.4	11 447	3.17×10^7	6397
2kpc_X_B	2.0	Stellar + XRay SED	27.89	2.5	4883	6.26×10^6	7677
4kpc_X_B	4.0	Stellar + XRay SED	31.19	4.9	2170	1.58×10^6	2882

Notes. Each model is run with the radiation source at an initial distance from the centre of the collapsing halo of 1.0, 2.0 and 4 kpc (physical). The initial distance is the distance at $z = 40$. For each of these models the spectrum is varied between a stellar SED (maximum photon energy = 60 eV and indicated with a '_S' in the name) and a stellar + XRay spectrum (indicated by an '_X' in the name). The soft X-ray spectrum has energies up to ∼380 eV while the models including hard X-rays have energies up to ∼7500 eV (the simulations including hard X-rays have an '_HX' in their name). All distances are in physical kpc unless explicitly stated. The core mass in the final column denotes the baryonic mass inside a 1 pc radius around the densest point.

of the models used for our two realizations. The name of the simulation is made up as follows: <InitialSeparation> _ <SpectraType> _ <Realisation> where for SpectraType 'S' stands for stellar only, 'X' stands for soft X-ray and 'HX' stands for hard X-ray.

3 RESULTS

3.1 The impact of soft X-rays

In order to properly assess the impact of the soft X-ray radiation component we break the analysis down into three constituent parts. We begin by examining visually the impact of the X-rays. We then analyse the impact of the X-rays by profiling the gas outwards from the point of maximum density back to the source, and finally we investigate the surrounding envelope of gas and look for effects at these larger scales.

3.1.1 Visual inspection

In Figs 2 and 3 we show a projection of Halo B for first when the halo is exposed to a stellar spectrum only and then in the following plot when the Halo is exposed to a stellar plus soft X-ray spectrum. Visually Halo A and Halo B are very similar, we choose to show Halo B simply because there is more overall structure in the region surrounding this halo. The projections are made at the final output time in both cases. The first item to notice is that the gas is much hotter and also much more diffuse in Fig. 3 compared to Fig. 2. The soft X-ray component is able to heat more of the gas to higher temperatures compared to the stellar only case. The gas in the model exposed to soft X-rays is also much more diffuse, looking at the gas number density projection shown in the bottom left panel there is an obvious lack of structure in the halo compared to the case where only a stellar spectrum is used. For the stellar model multiple high density structures exist with several density peaks clearly visible.

The right-hand panels of Figs 2 and 3 show the H_2 fraction (top) and electron fraction (bottom), respectively. X-rays should produce more free electrons at larger scales because of their greater mean free paths while the ionizing radiation will produce more free electrons local to the source. This is precisely what we see.

3.1.2 Ray profiles – flux statistics

In Fig. 4 we show the intensity in units of J_{21}.[8] We define the intensity, J, exactly as we defined it in R16:

$$J' = \sum_{E,i} \frac{k_i E}{4\pi^2 \sigma_i(E)} \tag{9}$$

$$J = \frac{J'}{\nu_H J_{21}} \tag{10}$$

where J' is the sum of the intensities for each species, i, over all energy bins, E. Here k_i is the number of photoionizations (or dissociations) per second for species i, $\sigma_i(E)$ is the cross-section for species i at energy E. Finally, $\nu_{\rm H}$ is the frequency at the hydrogen ionization edge. The extra factor of π in the denominator accounts for the solid angle. The output is taken from Halo A when the initial separation is set to 1 kpc i.e. simulations 1kpc_S_A, 1kpc_X_A and 1kpc_HX_A. The profile is determined by averaging over 10 line-of-sight rays, each starting from the point source but each ray is given a small angular offset and so each ray travels along a slightly offset path to a circular region surrounding the point of maximum density. One of the 10 rays is exactly along a ray joining the source and point of maximum density, using a small number of rays means there is a weighting towards this line while still displaying an overall average. We break the radiation intensity into components below the ionization threshold of hydrogen and those above the ionization threshold. The solid lines show the radiation in the infrared (IR) and Lyman–Werner (LW) bands while the dashed lines show the radiation intensity for energies greater than 13.6 eV. The black line shows the intensity for the stellar only model, the red line shows the intensity for the soft X-ray model while the green line

[8] J_{21} is defined as 10^{-21} erg cm^{-2} s^{-1} Hz^{-1} sr^{-1}.

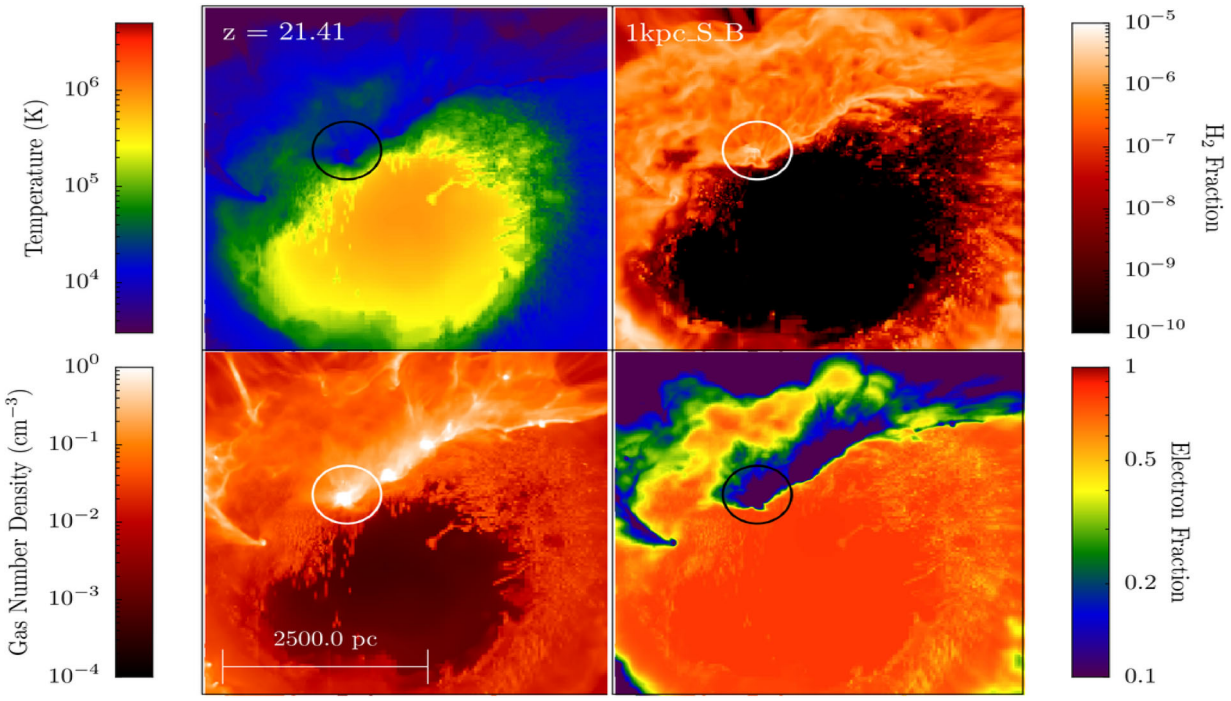

Figure 2. HaloB: stellar SED. Top left panel – temperature, top right panel – H_2 fraction, bottom left panel – gas number density, bottom right panel – electron fraction. This visualization is created by projecting through a cuboid with dimensions of 2500, 1250, 2500 pc centred on the point of maximum density. The projection is made along the *y*-axis. The output is the final output time from the 1kpc_S_B simulation. The heart shaped region created by the ionizing source is clearly visible in each panel. The black or white circle in each panel indicates the position of maximum density, the radius of the circle corresponds to the virial radius of the collapsing halo. Each panel is centred on the position of the radiating source at this output time.

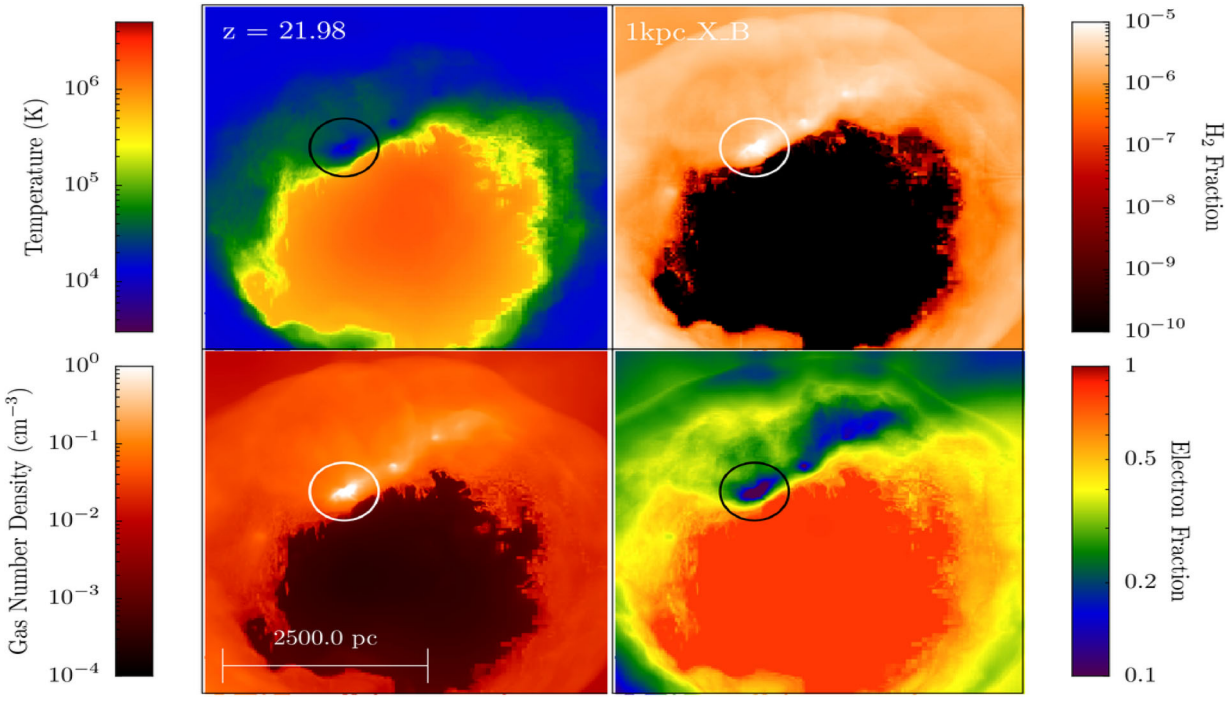

Figure 3. HaloB: Stellar + XRay SED. Top left panel – temperature, top right panel – H_2 fraction, bottom left panel – gas number density, bottom right panel – electron fraction. Same as Fig. 2 for simulation 1kpc_X_B.

shows the contribution from the hard X-ray model. The LW and IR intensities are identical in all cases as expected with a value of a few times J_{21} in the core. This part of the spectrum is not affected by the inclusion of X-rays. However, the ionizing components are quite different between the stellar and X-ray cases. The ionizing radiation from the stellar source is much less penetrating and is effectively blocked at a radius of ∼100 pc. However, for the soft X-ray spectrum we are able to penetrate much more deeply into

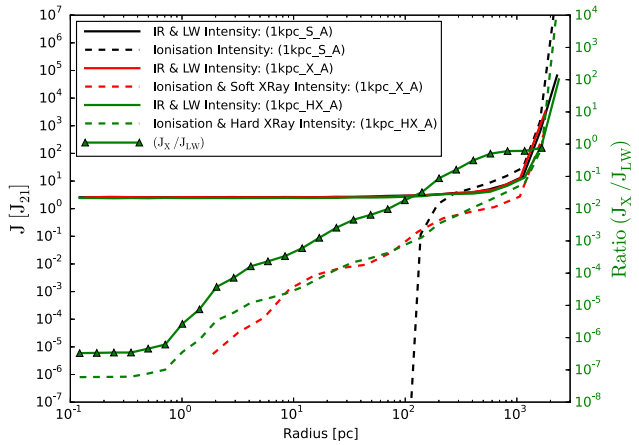

Figure 4. HaloA: the intensity ray profile for radiation emitted at a distance of 1 kpc (initially) from the collapsing halo. The intensity is broken into components below the ionization threshold of hydrogen (IR and LW) and that above the threshold. The black line refer to the simulation using a stellar spectrum only. The red line is from a simulation with a stellar plus soft X-ray flux and the green line includes in addition also a hard X-ray flux. Radiation below 13.6 eV is able to penetrate deep into the halo with only minimal self-shielding. The ionizing radiation however suffers from varying degrees of absorption depending on the frequency of the radiation. On the right-hand axes we show the values of the ratio between the X-ray radiation and the IR and LW radiation for the hard X-ray spectrum model. The X-ray intensity is always sub-dominant to the IR and LW radiation and drops sharply as the X-ray radiation is absorbed within approximately 100 pc of the centre.

the halo and in-fact can almost penetrate into the core of the halo - reaching down to a scale of ∼2 pc.

What is also clearly noticeable here is that the ionizing intensity of the soft X-ray spectrum drops sharply as the rays penetrate into the halo and has fallen by approximately six orders of magnitude compared to the IR and LW intensities at small scales. In-fact over the range from a radius of 1000 pc down to ∼1 pc the ionizing intensity for the soft X-ray spectrum drops from an intensity of ∼1 J_{21} down to $\sim 10^{-6}$ J_{21}. The green line with triangles as markers shows the ratio of the X-ray intensity (J_X) to the IR and LW intensity ($J_{\rm LW}$) for the hard X-ray spectrum model. The values of the ratio are labelled on the right hand axes. The fall in the ratio of J_X to $J_{\rm LW}$ is clearly apparent as absorptions of the X-ray component take effect. This is a direct consequence of both the $1/r^2$ dependence of the radiation field and the impact of absorptions along the line of sight. The inclusion of hard X-rays does little to change the intensity values, the only significant impact of the hard X-rays is that they are able to penetrate to even smaller scales reaching well into the core of the proto-galaxy.

When comparing the results found here with those elsewhere in the literature (e.g. Inayoshi & Omukai 2011; Hummel et al. 2015; Inayoshi & Tanaka 2015; Latif et al. 2015) it is important to bear this dependence in mind as other work has generally assumed a fixed relationship between the IR & LW intensity and the ionizing/X-ray intensity which is clearly not going to be the case for nearby sources. We will come back to this point in Section 4.

3.1.3 *Ray profiles – thermal characteristics*

We now compare the profiles of the gas systematically across a broad range of realizations. In Fig. 5 we have plotted ray profiles for Halo A for the case of the stellar spectrum and the soft X-ray spectrum. In this case 1000 rays are used to construct the profiles. If we begin by examining the temperature plot (lower left panel) we can see that the solid curves depicting runs with soft X-rays all show a significantly higher temperature at scales greater than

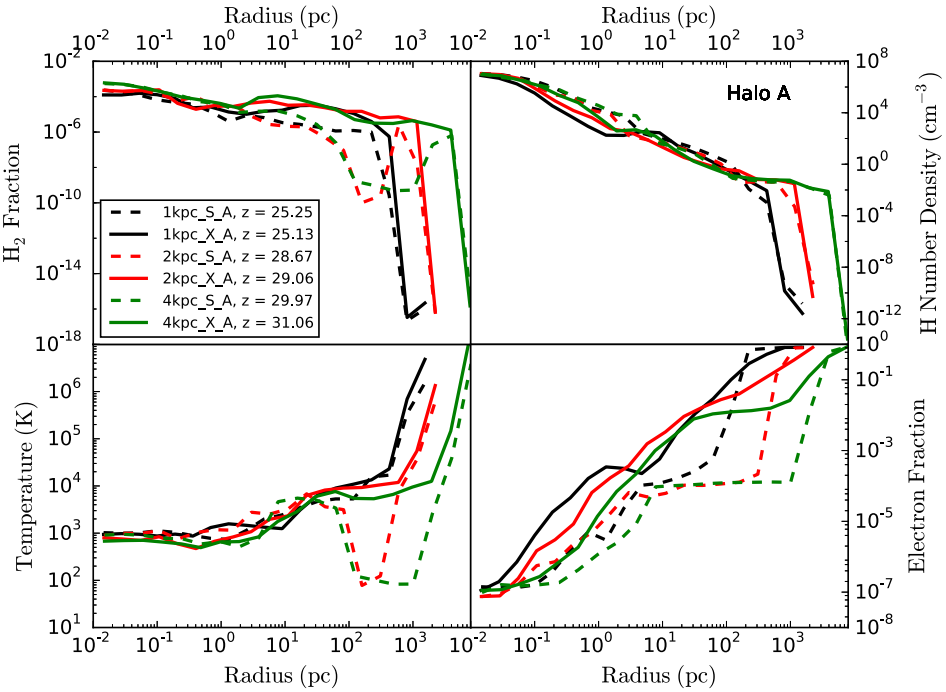

Figure 5. HaloA: ray profiles for Halo A at the final output time. The panels starting from the top left and moving clockwise are: H_2 fraction, neutral hydrogen density, electron fraction and temperature. Included in each panel are simulations having a stellar only spectrum and those containing a stellar plus soft X-ray spectrum. The stellar only simulations are indicated with an 'S' suffix and those with the stellar plus soft X-ray spectrum with an 'X' suffix. Each profile is shown at the final output time.

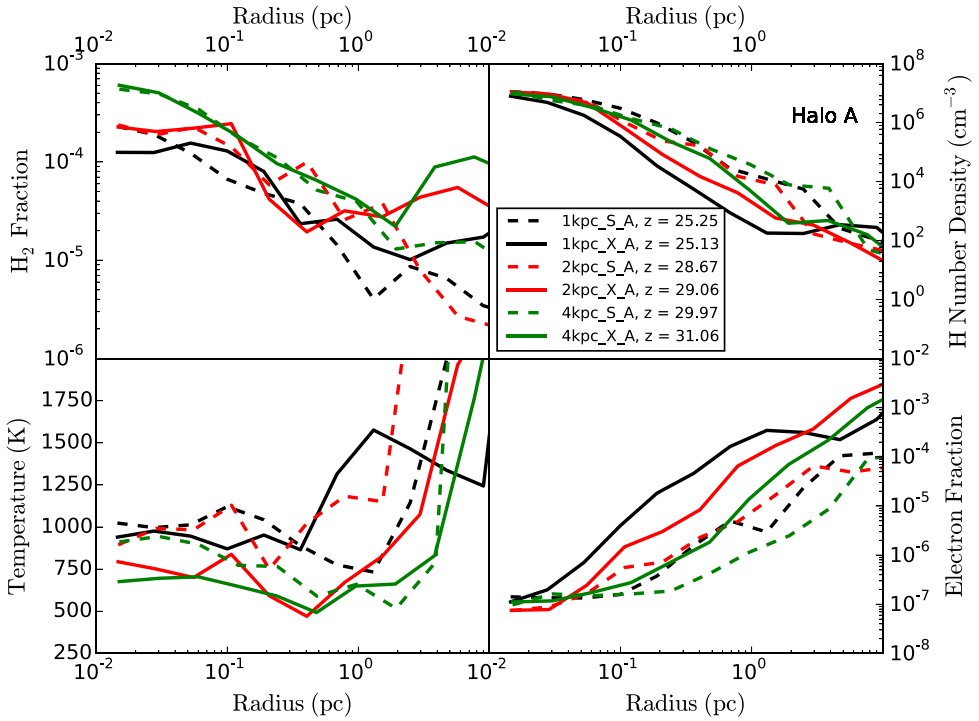

Figure 6. HaloA (Zoom): the same as Fig. 5 except that the region of interest has been set to between 0.01 and 10 pc. The scale on the temperature plot has been changed to a linear scale on the *y*-axis so that the temperature in the centre of the halo is clearly seen and the impact of the different spectra more clearly identifiable.

$\gtrsim$100 pc. The solid curves are those due to the soft X-ray spectrum and so the higher temperatures are due to the increased heating effects of the X-rays. At smaller scales the differences between the simulations are difficult to identify and we will inspect this region more closely in Fig. 6. Looking next at the top left panel the H_2 fraction is consistently higher for the simulations which include a soft X-ray component. This can be understood in terms of the gas chemistry, the X-rays induce more ionizations thereby increasing the free electron fraction (see the lower right panel for confirmation of this) which generates more H_2 via the two step Solomon process. The top right panel shows the neutral hydrogen density and agrees well with what we saw in Fig. 4.

To get a better quantitative picture of what the impact of the soft X-rays is on the central object forming at the centre of the halo we now zoom into the central 10 pc region and examine the same quantities at smaller scales where the differences in the spectrum may impact on what type of object could finally form in such a region. In Fig. 6 we show the region within 10 pc for Halo A while in Fig. 7 we show the same region for Halo B. All of the ray profiles are created from the final output time. Rigid systematic differences are not obvious as both the distance is changed and the spectrum is changed from stellar to stellar plus X-rays. However, some trends are none the less still clear.

(i) For the stellar spectrum only, as the distances are decreased the temperature in the centre increases in both cases albeit more for Halo B (∼30 per cent) than Halo A (∼10 per cent). This is because the H_2 fraction is highest in the cases where the radiation source is furthest from the collapsing halo. This is an obvious consequence of the r^{-2} dependence of the LW radiation field. Less H_2 is destroyed by the sources which are further away.

(ii) When the X-rays are included, the temperature in the core in all cases decreases by approximately 10 per cent. The H_2 fractions in the core are comparable for Halo A between the stellar and X-ray case while for Halo B the H_2 fractions are higher for the X-ray case. The higher H_2 fractions does, at least for Halo B, induce some extra cooling in the core as a result.

(iii) We do not find that soft X-rays cause the haloes to collapse earlier as a general rule. When comparing the impact of soft X-ray radiation to stellar radiation we find that in 2 out of 6 cases the halo collapses later. Naively one might expect the X-rays to generate more H_2 at low and intermediate densities which overcomes any heating effects to promote an earlier collapse time (compared to the stellar only case). However, we find this is not always true and rather the complex interplay between X-ray heating, H_2 formation, LW photodissociation and IR photodetachment means that the collapse and also the collapse time is somewhat chaotic. However, as we will see explicitly later the X-rays do result in less massive cores.

Outside of 1 pc the H_2 fraction for the cases where the X-rays are included can easily be an order of magnitude higher when compared to the stellar only case. However, as we profile into the core of the halo these differences become less pronounced and the H_2 fractions tend to converge towards the stellar only result. However, the convergence is not perfect and differences can exist between the stellar result and the soft X-ray result. This is clearest in the 1kpc_X_B case where the H_2 differs by a factor of more than two in the centre between the two spectra – although this still only leads to a temperature difference of the order of 10 per cent.

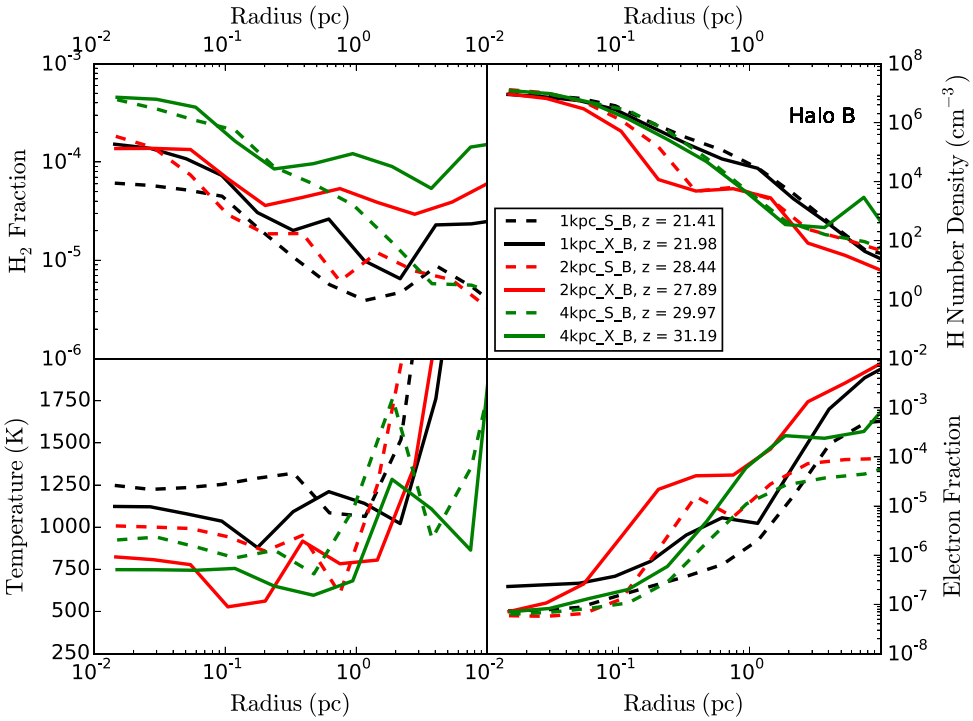

Figure 7. HaloB (Zoom): a zoomed in ray profile for Halo B with the horizontal radius scale again set to between 0.01 and 10 pc. Similar to Fig. 6.

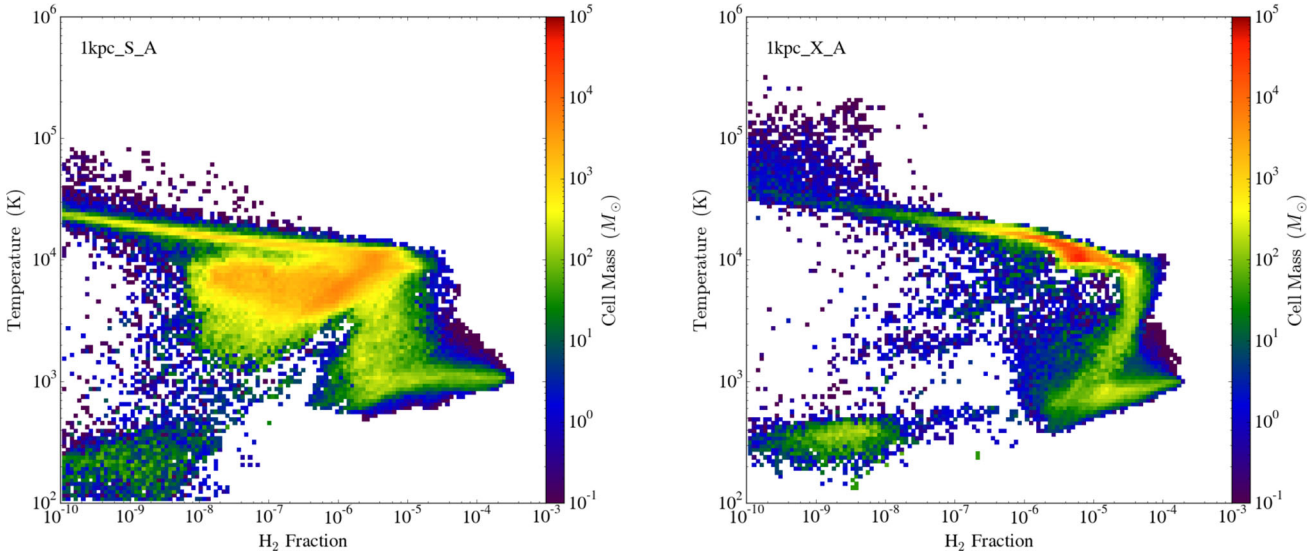

Figure 8. Halo A: phase diagram of H_2 fraction versus temperature weighted by enclosed cell mass. The left-hand panel is for the stellar only model at an initial separation of 1 kpc, the right-hand panel for the stellar plus soft X-ray model at an initial separation of 1 kpc. The X-rays produce a tighter relationship between H_2 and temperature by heating the gas and not allowing the gas to cool as efficiently forcing the gas to remain on the atomic cooling track until higher H_2 are reached. The gas masses in the bottom left corner of each plot is low density gas beyond the edge of the H II regions which is cool and has a depleted H_2 fraction.

3.2 The surrounding envelope and accretion rates

In Fig. 8 we examine the distribution of H_2 as a function of temperature weighted by cell mass. We only show the results from Halo A as the results from Halo B are qualitatively very similar. In the left-hand panel we show the output from Halo A at the final output time when only a stellar spectrum is used, in the right-hand panel we show the final output time for the case of a stellar plus soft X-ray spectrum. Visually the difference are quite striking, the stellar only model has a much broader distribution of gas in terms of temperature and to a lesser extent in the H_2 fraction. The stellar model has a large mass of gas between $T \sim 10^3$ K and $T \sim 10^4$ K with a H_2 fraction between 10^{-8} and 10^{-5}. The model including X-rays however has much narrower temperature distribution with most of the gas sitting at $T \sim 10^4$ K even though the H_2 fraction is actually higher at values between 10^{-7} and 10^{-4}. However, the

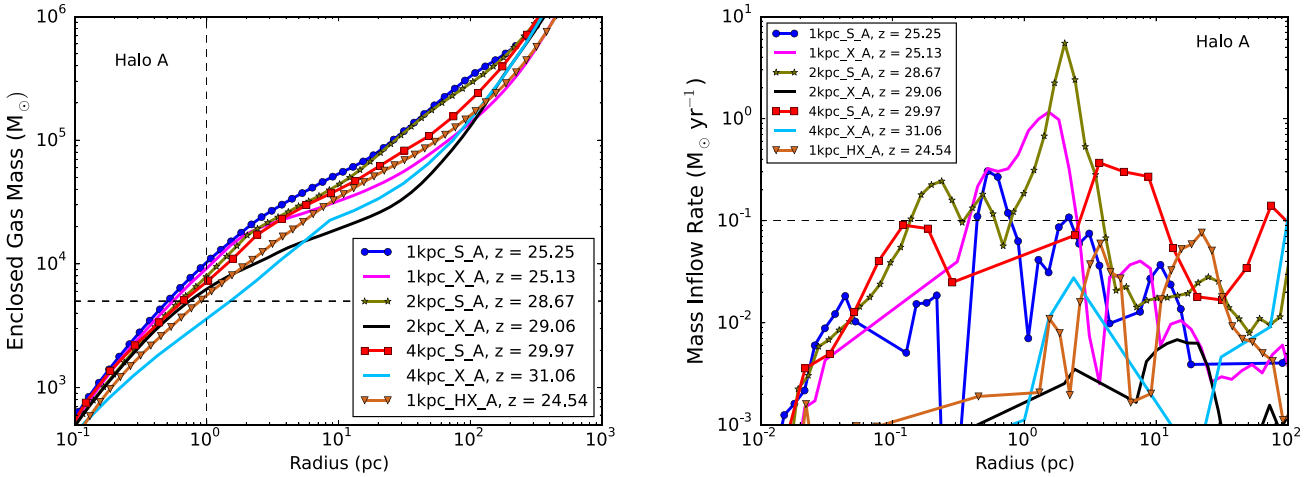

Figure 9. Radial profiles for HaloA. The left-hand panel shows the enclosed mass profile from 0.1 pc up to 1000 pc. The deleterious effects of the X-rays are most noticeable in this case for the models in which the initial separation is greater than 1 kpc, in the 2kpc_X_A and 4kpc_X_A the halo collapses earlier and the enclosed mass is reduced significantly. The right-hand panel shows the accretion rates from 0.01 pc to 100 pc out from the maximum density. The dashed line at a mass inflow rate of 0.1 $M_\odot$ yr^{-1}, is shown as approximately the mass inflow rate required to produce an SMS.

heating effects of the X-rays at this close separation means that the bulk of the gas is heated to 10^4 K with the increased H_2 fraction and the increased associated cooling being unable to counteract the heating effect.

This increased temperature of the gas when exposed to X-rays, most especially the gas at scales greater than 10 pc, means that the enclosed mass fraction is always higher at a given scale for gas exposed to a stellar only spectrum compared to an X-ray spectrum. In the left-hand panel of Fig. 9 we show the enclosed mass as a function of radius for Halo A. The enclosed mass is greatest when the source is closest to the collapsing halo and when it is exposed to stellar photons only. X-rays show a systematic reduction in the enclosed mass when compared to the stellar spectrum which becomes more pronounced as the distance to the source increases. This is because the LW radiation disrupts H_2 cooling effectively when the flux is strongest (closest) and the ionizing radiation is not as efficient at heating the gas compared to X-rays at these scales. Hence, the H_2 fraction is lowest when the source is closest and for the stellar spectrum resulting in a larger enclosed mass collapsing. The same mechanism also has an effect on the mass in-flow rates, albeit weaker, as shown in the right-hand panel of Fig. 9. For the larger separations with X-rays we see that the mass inflow rates are quite low. This is because the X-rays heat the gas reducing its ability to cool and thus leads to lower infall rates. However, at a 1 kpc separation the accretion rate, even in the X-ray case, is very high. In fact for the X-ray case at a separation of 1 kpc the peak mass inflow rate exceeds the stellar case. What is clear is that the increased temperature of the gas, compared to the stellar case, results in a reduced mass inflow rate and that X-rays at separations of 2 kpc or more give the lowest mass inflow rates. However, when the separation drops to 1 kpc the negative H_2 inducing impact of the X-rays disappears and the impact of the X-rays becomes neutral and may even switch sign to being marginally positive.

The formation of SMS is postulated when the accretion rates on to a central object can exceed $\sim$0.1 $M_\odot$ yr^{-1} (Begelman, Volonteri & Rees 2006; Johnson et al. 2012; Hosokawa et al. 2013; Schleicher et al. 2013). Our mass inflow rates peak at values much larger than 0.1 $M_\odot$ yr^{-1} for the nearby radiation sources. Assuming a lifetime of $\sim$1 Myr for such a massive star and an initial mass of $M_{\rm init} \sim 10^4$ $M_\odot$ the star could grow to a mass exceeding a few times 10^5 $M_\odot$ by the end of its short lifetime. More in-depth simulations, which are beyond the scope of this study, of the continued evolution of this particular collapse would be required to support this hypothesis. Such a simulation would need to include detailed stellar evolution modelling of SMS formation (e.g. Hosokawa et al. 2011; Hosokawa, Omukai & Yorke 2012; Hosokawa et al. 2013; Inayoshi, Omukai & Tasker 2014).

3.3 Does a hard X-ray spectrum make any difference?

In Fig. 10 we show the impact of hard X-ray photons on the gas state when compared to the soft X-ray models. The hard X-ray models are described in Table 2. The hard X-ray models increase the number of energy bins required from 8 to 11 and the subsequent runtime increases significantly (the 1kpc_HX_A run took more than 60 d (wall-clock time) to complete ($\sim$370 000 CPU h) compared to an average runtime of 10 d ($\sim$62 000 CPU h)). As a result the hard X-ray model was only run for Halo A. The mean free path of the hard X-rays is longer than for the soft X-rays as their interaction cross-section is smaller. This feature is also confirmed in Fig. 4 where we see that the intensity due to hard X-rays is almost identical to soft X-rays but with a deeper penetration (this was for an initial separation of 1 kpc in each case).

In the bottom left panel of Fig. 10 we see that hard X-rays (solid lines) have little impact on the temperature of the gas compared to the soft X-ray case for the 2 kpc and 4 kpc cases. For the case of the 1 kpc separation the temperature of the gas in the core of the halo is approximately 300 K lower compared to the soft X-ray case. We have over-plotted the enclosed gas mass and mass inflow rates for the 1kpc_HX_A runs in Fig. 9. It is clear from this figure that the enclosed mass values for the 1kpc_HX_A run is much lower than both the 1kpc_S_A and 1kpc_X_A runs at distances up to $\sim$100 pc from the centre. This trend is confirmed by the mass inflow values in the right-hand panel. The reason for the reduced enclosed mass values is due to the variation in the penetrating ability of the photons as a function of their energies. More energetic photons are able to ionize the hydrogen to greater depths, suppression gas accretion and reducing the enclosed mass.

As a result we see higher enclosed masses for the stellar only case compared to the soft X-ray case, for which the masses are

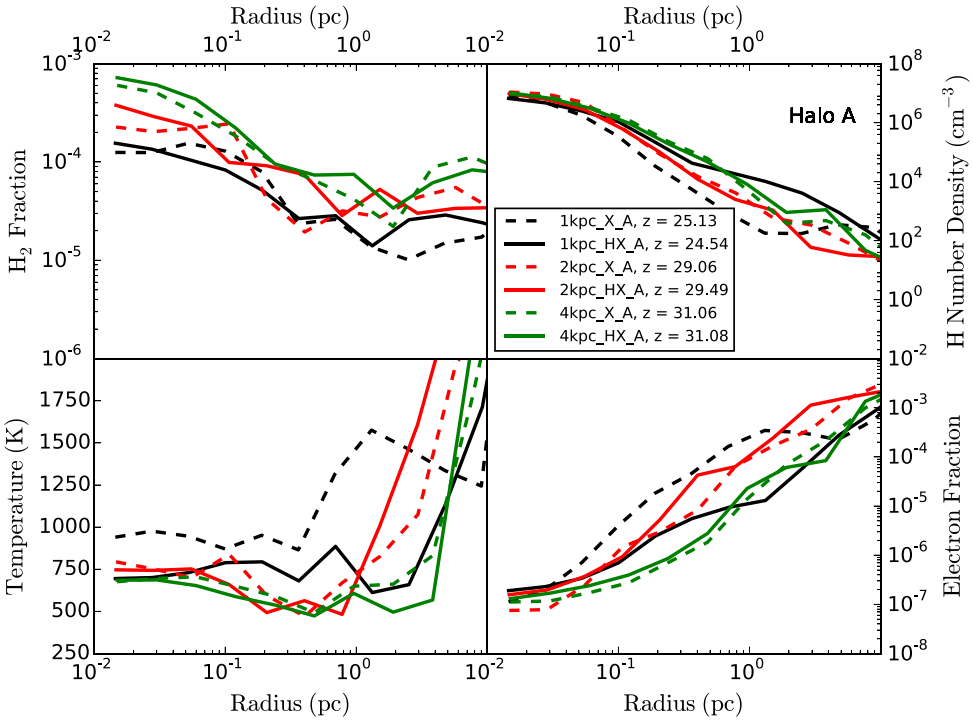

Figure 10. HaloA (HardXRays): this figure shows ray profiles for the cases where soft X-ray and hard X-ray models are used. The hard X-ray models differ only in that photons with energies $\gtrsim$1 keV are included in the model. The inclusion of hard X-rays has only a small effect on the gas quantities for the cases where the separation is greater than 1 kpc. For the 1 kpc realization the temperature is approximately 300 K lower in the hard X-ray case compared to the soft X-ray case but it is consistent with the other profiles.

again higher when compared to the hard X-ray case at a radius of $\lesssim$ 10 pc. The effect is somewhat cumulative, while soft X-rays do certainly induce a small negative effect here the hard X-rays enhance it to significant levels.

We have explicitly compared this effect in Fig. 11 where we have taken the 1 kpc models and compared them as their spectrum is varied. We saw in Fig. 9 that the enclosed mass values are connected to the penetrating ability of the ionizing photons. In the left-hand panel of Fig. 11 we see that the stellar spectrum photons get halted at a radius of $\gtrsim$100 pc, the soft X-ray photons at closer to 1 pc and the hard X-ray photons make it all the way into the core. It is the extra ionization caused by the hard X-rays which further suppresses the mass inflow rate compared to the soft X-ray and stellar case and hence the enclosed mass.

Latif et al. (2015) investigated the impact of hard X-rays photons (uniform background X-ray intensities of between $J_X = 0.01$ and $J_X = 1.0$)[9] and found that the hard X-rays increase the value of $J_{\rm crit}$ by a factor of between 2 and 4. Their values of the X-ray intensities are significantly beyond what we simulate here, and more appropriate for the X-ray spectrum expected for nearby accreting SMBHs.

In summary we find that hard X-rays from realistic sources have an additional negative effect compared to soft X-rays. Their ability to penetrate deep into a halo and ionize hydrogen leads to less centrally concentrated gas clouds, leading to lower core masses.

[9] $J_X = J_{X,21}(\frac{\nu}{\nu_0})^{-1.5}$ and $J_{X,21}$ is the Cosmic X-ray background flux in units of J_{21}

4 DISCUSSION

Disrupting or preventing completely the formation of H_2 is seen as a necessary criteria for the direct collapse model of SMBH formation. As a result nearby, strongly luminous, galaxies which produce copious amounts of Lyman–Werner radiation are seen as a vital component. It is however, also clear that these galaxies will form at least some HMXBs which will lead to a significant X-ray component on top of the stellar component. In this work we have investigated thoroughly the added impact of both soft and hard X-rays compared to a stellar only spectrum.

There has been some debate in the literature as to the feedback effects of X-rays on SMBH formation. Hummel et al. (2015) investigated the effect of Population III star formation under X-ray feedback. They found that the gas becomes optically thick to X-rays at densities above approximately $n_H \sim 10^4$ cm^{-3} and that as a result Pop III star formation is relatively insensitive to the presence of a cosmic X-ray background. Inayoshi et al. (2015) came to a slightly different conclusion in the context of direct collapse black holes. They found that the impact of soft X-rays is to increase the value of $J_{\rm crit}$ thus making DCBH formation less likely. In their study they set the intensity of X-rays to approximately 10^{-5} times that of the LW intensity (see their equation 14). They find that the critical LW intensity required for direct collapse is increased by at least an order of magnitude when X-ray intensities of $J_X \gtrsim 0.01$ are included. However, their results are not for a single source and instead they consider a much larger far ultraviolet flux (which could be due to multiple nearby haloes) and scale the X-ray flux proportionately. As such they investigate a somewhat different scenario to that of a single dominant source. By comparison we evolve the radiation field self-consistently in 3-D. In Fig. 4 we see a very strong decrease

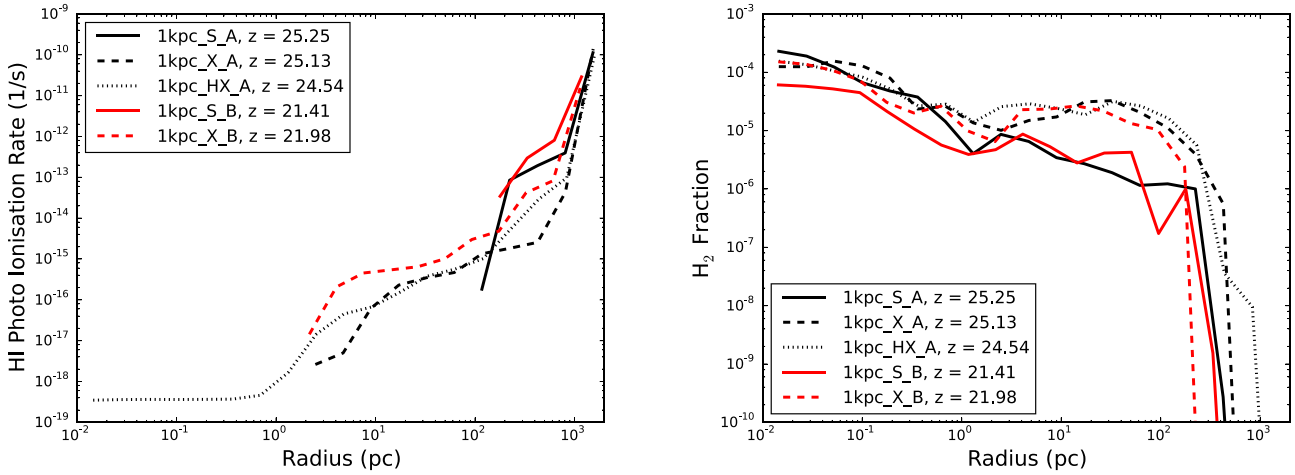

Figure 11. 1 kpc models: the two panels show ray profiles for all of the models where the initial separations is 1 kpc. Black for Halo A and red for Halo B. Solid lines for the stellar spectra, dashed for the soft X-rays and dotted for the hard X-ray models. In the left-hand panel we see that the models including X-rays show significantly more ionizing ability. In the right-hand panel the strong increase in H_2 fraction between 3 and 300 pc is clear for the X-ray case. However, this increased H_2 fraction does not lead to a temperature reduction as the heating effects of the X-rays dominate at these densities.

in the X-ray intensity compared to the LW intensity as we move towards the centre of the collapse. It is this variation in the X-ray intensity with distance that will ultimately determine the feedback effects from the X-rays as we discuss below.

Our detailed modelling shows that (similar to Hummel et al. 2015) the inner regions of the halo are agnostic to the X-rays and hence the thermal characteristics of the gas are relatively insensitive to the X-ray component. We see only small changes in the thermal characteristics of the core of the halo with the inclusion of X-rays. The impact is especially small when the initial separation is small and only grows slightly as the X-ray source is moved further away.

However, X-rays do have a significant effect on the gas surrounding the core i.e. gas between 1 pc and a few times 10^2 pc from the central maximum. As the X-ray source is moved further from the halo we see the gas in the envelope surrounding the core is negatively affected. The negative feedback effects of the X-rays are seen clearly in terms of the enclosed mass of the halo and more weakly, in the mass inflow rates. This distance dependence can be understood in terms of the effect of the X-rays on the low and medium density gas in particular (i.e. gas at a density of $n_H \lesssim 10^2$ cm^{-2}). The X-rays, compared to the stellar only case, result in more diffuse gas which is much hotter than the gas in the stellar only case (see Fig. 5). For the cases where the separation is 2 kpc and 4 kpc, respectively, the gas is approximately two orders of magnitude hotter in the X-ray case leading to significantly reduced accretion rates and hence smaller core masses.

In the range $r = 3$–300 pc (see for example Fig. 11 right-hand panel), the H_2 fraction increases by an order of magnitude when X-rays impact the system, which partially ionize the outer parts of the halo. We can estimate the equilibrium H_2 fraction by setting the H_2 formation time $t_{\rm form} \approx f(H_2)/k_{H^-} n_b f(e^-)$ to its dissociation time $t_{\rm diss} = k_{\rm diss}^{-1} = 23/J_{21}$ kyr (Yoshida et al. 2003; Wise & Abel 2007), arriving at $f_{\rm eq}(H_2) \simeq (23\ {\rm kyr}/J_{21}) k_{H^-}\ n_b\ f(e^-)$. Here $f(i)$ is the fractional abundance of species i, $n_b = 10$ cm^{-3} is the baryon number density and k_{H^-} is the H^- formation rate coefficient by electron photoattachment and is around 10^{-15} cm^3 s^{-1} at $T \approx 1000$ K (Wishart 1979; Glover & Abel 2008). Taking the conditions at $r \simeq 10$ pc in 1kpc_X_A, the equilibrium abundance $f_{\rm eq}(H_2) \simeq 2 \times 10^{-5}$, in line with (or perhaps slightly above) the simulation data. Because $f_{\rm eq}(H_2)$ scales with electron fraction, both the electron and H_2 fraction drop by a factor of 10 in the stellar-only run. At this scale the electrons are in ionization equilibrium. Comparing the recombination rate to the ionization rate at the hydrogen edge leads us to an equilibrium value of $f(e^-) \sim 4 \times 10^{-3}$ in the case of X-rays and $f(e^-) \sim 7 \times 10^{-4}$ for the stellar case. The free electron fraction in the stellar case reaches a plateau (see Fig. 5) of $f(e^-) \sim 1 \times 10^{-4}$ between scales of $r \simeq 10$ pc and $r \simeq 1000$ pc which is its collisional equilibrium value as opposed to its photoionization value seen in the case of X-rays. At any rate the heating effect of the X-rays dominates over any induced cooling effects from the enhanced H_2 fraction. We see no material effect from the slightly elevated H_2 fraction due to X-rays (compared to the stellar only case), rather the heating effect dominates and suppresses the accretion rates.

Inside of the cores, where densities are similar in both the stellar and X-ray cases the thermal characteristics are similar, the cores are simply less massive. For the case where the initial separation is 1 kpc the temperature profiles between the stellar and soft X-ray case are virtually identical leading to mass inflow rates which are very similar. In this case there is little negative impact due to the soft X-rays and in fact the mass inflow rates are slightly higher for the X-ray case. For a hard X-ray spectrum the photons can penetrate into the very core (see Fig. 11). As a result hard X-rays induce a negative feedback effect at all separations, which is likely to be detrimental to (massive) star formation in haloes exposed to such a spectrum.

A significant caveat to our study is that we examine the case of a single radiation source. We do not attempt to model classical DCBH formation in this study, instead we focus solely on studying the effect of nearby (X-ray) radiation sources which are seen as a cornerstone of creating pristine atomic cooling haloes and by extension are a cornerstone of the DCBH formation mechanism. While this allows us to disentangle the effects of a realistic radiation source from other nearby radiation sources it is unlikely to be the cosmologically realistic case. As we clearly showed in Section 3.1.3 a nearby radiation source with characteristics similar to a first galaxy is unable to fully dissociate H_2 in a collapsing halo (the effect of this non-negligible H_2 abundance on the gas thermo-dynamics is unclear – gas fragmentation may be one outcome – however, an investigation of the further evolution of the gas collapse is beyond the scope of this work). What will more likely be required is the

scenario where a nearby source is augmented by additional sources clustered around rare density peaks. These additional sources will sum to produce a background radiation field which will for a given time be dominated by one (as simulated here), or at most a handful of nearby sources. Our work should therefore be seen as an initial test of the closely separated pairs mechanism (Visbal et al. 2014b). Our simulations show that a single nearby source will likely *not* provide a sufficient condition for the formation of DCBH seed.

A recent study by Chon et al. (2016) uses the star particle technique together with a spatially and temporally varying LW radiation field including self-shielding to examine the conditions for direct collapse. They use a large volume (20 h^{-1} Mpc comoving) and include the effect of multiple sources finding multiple DC candidates. They conclude that while a nearby neighbour is required to provide a sufficiently intense LW radiation field the neighbour can also hamper the formation of an SMS through adverse dynamical interactions. In our study these dynamical effects are absent due to our chosen setup. Furthermore, Chon et al. (2016) find that the value of the LW intensity may not be as high as described more generally in the literature and may in fact be much lower than the often quoted value of $J_{\rm crit} \sim 1000\, J_{21}$ due to the presence of the near neighbour and the variation in the flux (and increase in the flux as the haloes merge). We have specifically not simulated a nearby host with the intention of trying to uncover a single value for '$J_{\rm crit}$' but rather we focus on examining the case of a single galaxy with star formation rates and masses deemed likely at this redshift.

5 CONCLUSIONS

We have studied here the effects of X-ray feedback on forming direct collapse black hole seeds. Our conclusions are as following.

(i) *The incorporation of X-rays has a negligible effect on the thermal profile of the core of the halo*. The core of the halo feels only a very minimal effect from the X-rays due to self-shielding. At scales below approximately 1 pc the thermal profiles of all of our simulations look quite similar. The haloes irradiated by X-rays do show small increases in the H_2 fraction within the core and this does lead to a small reduction in the core temperature at the level of $\lesssim$10 per cent but the overall effect is small.

(ii) *There is a strong distance dependence of the X-ray source which severely affects the enclosed mass of the collapsing core. Nearby X-ray sources have a smaller negative impact compared to those at larger distances*. X-ray sources at distances between 1 kpc and 4 kpc all reduce the enclosed mass found within the core of the collapsing halo compared to the stellar only case. The level of reduction is dependent on the distance to the source. We found that sources at a distance of 1 kpc suffered approximately a 10 per cent reduction in enclosed mass while those at distance of 4 kpc suffered a reduction of ∼50 per cent. The distance dependence is a result of the heating effects of the X-rays which results in more diffuse gas and smaller mass inflow rates. Cold gas which is surrounding the halo when the halo is exposed to only stellar photons is heated by the X-rays reducing mass inflow.

(iii) *The H_2 formed by the extra free electrons due to X-rays has no material impact on the thermodynamics outside the core*. Instead the heating effects of the X-rays are the dominant component. At a distance of ∼100 pc from the central density we see more H_2 in the X-ray compared to the stellar case but the gas is also significantly hotter (see Fig. 5). The cold gas available for accretion in the stellar case has been heated in the X-ray case. This is especially true for sources at an initial separation of 2 kpc or greater and hence the larger negative feedback effects in this case.

(iv) *Hard X-ray photons from nearby sources can have an additional negative impact*. We found that for initial separations of 2 kpc and 4 kpc the inclusion of hard X-rays had a negligible effect on our results and that their thermal characteristics matches closely that of the soft X-ray models. The source at an initial separation of 1 kpc (1kpc_HX_A model) resulted in a lower temperature core and a much lower enclosed mass. This reason for this is that the increased hydrogen ionizing ability of the hard X-rays in the denser regions of the halo suppresses further the mass inflow rate. The increased electron fraction also provides additional H_2 causing a slightly lower temperature core, though this effect is small as discussed above. Overall, we find that at very close separations hard X-rays have an additional negative feedback effect compared to soft X-rays. However, HMXBs accreting at rates comparable to the Eddington rate (say 10 per cent Eddington) will produce far more soft X-ray photons than hard X-ray photons. This is because HMXBs which are accreting due to Roche lobe overflow will lead to higher disc accretion rates and hence a spectrum peaked at lower energies (e.g. Done et al. 2007). As a result the impact of soft X-ray feedback is likely to be more important in the context of DCBH seeds.

Hence, we conclude that because X-rays do reduce the enclosed mass within the core of the collapsing halo they can have a negative impact. In particular, and in agreement with previous studies, when the source of X-rays is sufficiently distant from the collapsing halo (much like a cosmic X-ray background) then there is likely to be a significant negative feedback effect on forming DCBHs. However, the caveat is that the negative impact diminishes as the distance to the source decreases. This is an important finding. It implies that for close halo pairs (Dijkstra et al. 2008; Agarwal et al. 2012; Dijkstra et al. 2014) or for so-called synchronized halo pairs (Visbal et al. 2014b) in an otherwise fairly benign environment the negative feedback wrought by X-rays may not be significant due to their close separation. While this may further constrain the search for DCBH environments to those regions without a pervasive X-ray background this is likely to be the general case at high redshift. Furthermore, the result that sufficiently nearby sources of X-rays do not show significant negative feedback further strengthens the case for nearby luminous galaxies to be the catalyst for forming DCBHs.

ACKNOWLEDGEMENTS

JAR would like to thank Chris Done for fruitful and informative discussions on X-ray emission mechanisms. This work was supported by the Science and Technology Facilities Council (grant numbers ST/L00075X/1 and RF040365). This work used the DiRAC Data Centric system at Durham University, operated by the Institute for Computational Cosmology on behalf of the STFC DiRAC HPC Facility (www.dirac.ac.uk). This equipment was funded by BIS National E-infrastructure capital grant ST/K00042X/1, STFC capital grant ST/H008519/1, and STFC DiRAC Operations grant ST/K003267/1 and Durham University. DiRAC is part of the National E-Infrastructure. JAR and PHJ acknowledge the support of the Magnus Ehrnrooth Foundation, the Research Funds of the University of Helsinki and the Academy of Finland grant 1274931. JHW acknowledges support by NSF and NASA grants AST-1333360, HST-AR-13895.001, and HST-AR-14326.001. Some of the numerical simulations were also performed on facilities hosted by the CSC -IT Center for Science in Espoo, Finland, which are financed

by the Finnish ministry of education. Computations described in this work were performed using the publicly available ENZOcode (http://enzo-project.org), which is the product of a collaborative effort of many independent scientists from numerous institutions around the world. Their commitment to open science has helped make this work possible. The freely available astrophysical analysis code YT (Turk et al. 2011) was used to construct numerous plots within this paper. The authors would like to extend their gratitude to Matt Turk et al. for an excellent software package. JAR would like to thank Lydia Heck and all of the support staff involved with Durham's COSMA4 and DiRAC's COSMA5 systems for their technical support. Finally, the authors would like to thank an anonymous referee for a considered and detailed report which helped to improve both the clarity and quality of this manuscript.

REFERENCES

Abel T., Wandelt B. D., 2002, MNRAS, 330, L53
Agarwal B., Khochfar S., Johnson J. L., Neistein E., Dalla Vecchia C., Livio M., 2012, MNRAS, 425, 2854
Agarwal B., Davis A. J., Khochfar S., Natarajan P., Dunlop J. S., 2013, MNRAS, 432, 3438
Agarwal B., Dalla Vecchia C., Johnson J. L., Khochfar S., Paardekooper J. P., 2014, MNRAS, 443, 648
Alvarez M. A., Wise J. H., Abel T., 2009, ApJ, 701, L133
Begelman M. C., Volonteri M., Rees M. J., 2006, MNRAS, 370, 289
Bromm V., 2013, Rep. Prog. Phys., 76, 112901
Bromm V., Loeb A., 2003, ApJ, 596, 34
Bromm V., Yoshida N., 2011, ARA&A, 49, 373
Bruzual G., Charlot S., 2003, MNRAS, 344, 1000
Bryan G. L., Norman M. L., O'Shea B. W., Abel T., Wise J. H., Turk M. J., The Enzo Collaboration, 2014, ApJS, 211, 19
Chandrasekhar S., 1964, ApJ, 140, 417
Chen P., Wise J. H., Norman M. L., Xu H., O'Shea B. W., 2014, ApJ, 795, 144
Chon S., Hirano S., Hosokawa T., Yoshida N., 2016, preprint (arXiv:1603.08923)
Ciotti L., Ostriker J. P., 2001, ApJ, 551, 131
Clark P. C., Glover S. C. O., Klessen R. S., Bromm V., 2011, ApJ, 727, 110
Coppola C. M., Longo S., Capitelli M., Palla F., Galli D., 2011, ApJS, 193, 7
Coppola C. M., D'Introno R., Galli D., Tennyson J., Longo S., 2012, ApJS, 199, 16
Dijkstra M., Haiman Z., Mesinger A., Wyithe J. S. B., 2008, MNRAS, 391, 1961
Dijkstra M., Ferrara A., Mesinger A., 2014, MNRAS, 442, 2036
Done C., Gierliński M., Kubota A., 2007, A&AR, 15, 1
Fernandez R., Bryan G. L., Haiman Z., Li M., 2014, MNRAS, 439, 3798
Field G. B., Somerville W. B., Dressler K., 1966, ARA&A, 4, 207
Glover S. C. O., 2015a, MNRAS, 451, 2082
Glover S. C. O., 2015b, MNRAS, 453, 2901
Glover S. C. O., Abel T., 2008, MNRAS, 388, 1627
Glover S. C. O., Jappsen A. K., 2007, ApJ, 666, 1
Glover S. C. O., Savin D. W., 2009, MNRAS, 393, 911
Greif T. H., Springel V., White S. D. M., Glover S. C. O., Clark P. C., Smith R. J., Klessen R. S., Bromm V., 2011, ApJ, 737, 75
Hahn O., Abel T., 2011, MNRAS, 415, 2101
Hirano S., Hosokawa T., Yoshida N., Umeda H., Omukai K., Chiaki G., Yorke H. W., 2014, ApJ, 781, 60
Hosokawa T., Omukai K., Yoshida N., Yorke H. W., 2011, Science, 334, 1250
Hosokawa T., Omukai K., Yorke H. W., 2012, ApJ, 756, 93
Hosokawa T., Yorke H. W., Inayoshi K., Omukai K., Yoshida N., 2013, ApJ, 778, 178
Hummel J. A., Stacy A., Jeon M., Oliveri A., Bromm V., 2015, MNRAS, 453, 4136
Inayoshi K., Omukai K., 2011, MNRAS, 416, 2748
Inayoshi K., Omukai K., 2012, MNRAS, 422, 2539
Inayoshi K., Tanaka T. L., 2015, MNRAS, 450, 4350
Inayoshi K., Omukai K., Tasker E., 2014, MNRAS, 445, L109
Inayoshi K., Visbal E., Kashiyama K., 2015, MNRAS, 453, 1692
Johnson J. L., Bromm V., 2007, MNRAS, 374, 1557
Johnson J. L., Whalen D. J., Fryer C. L., Li H., 2012, ApJ, 750, 66
Kim J. h., Wise J. H., Alvarez M. A., Abel T., 2011, ApJ, 738, 54
Kim J. h. et al., 2014, ApJS, 210, 14
Kitsionas S., Whitworth A. P., 2002, MNRAS, 330, 129
Kuhlen M., Madau P., 2005, MNRAS, 363, 1069
Latif M. A., Schleicher D. R. G., Schmidt W., Niemeyer J., 2013, MNRAS, 433, 1607
Latif M. A., Bovino S., Van Borm C., Grassi T., Schleicher D. R. G., Spaans M., 2014a, MNRAS, 443, 1979
Latif M. A., Schleicher D. R. G., Bovino S., Grassi T., Spaans M., 2014b, ApJ, 792, 78
Latif M. A., Bovino S., Grassi T., Schleicher D. R. G., Spaans M., 2015, MNRAS, 446, 3163
Mayer L., Fiacconi D., Bonoli S., Quinn T., Roškar R., Shen S., Wadsley J., 2015, ApJ, 810, 51
Milosavljević M., Couch S. M., Bromm V., 2009, ApJ, 696, L146
Mirocha J., Skory S., Burns J. O., Wise J. H., 2012, ApJ, 756, 94
Mitsuda K. et al., 1984, PASJ, 36, 741
Mortlock D. J. et al., 2011, Nature, 474, 616
Oh S. P., Haiman Z., 2002, ApJ, 569, 558
Omukai K., 2001, ApJ, 546, 635
Planck Collaboration XVI, 2014, A&A, 571, A16
Regan J. A., Haehnelt M. G., 2009a, MNRAS, 393, 858
Regan J. A., Haehnelt M. G., 2009b, MNRAS, 396, 343
Regan J. A., Johansson P. H., Haehnelt M. G., 2014a, MNRAS, 439, 1160
Regan J. A., Johansson P. H., Wise J. H., 2014b, ApJ, 795, 137
Regan J. A., Johansson P. H., Wise J. H., 2015, MNRAS, 449, 3766
Regan J. A., Johansson P. H., Wise J. H., 2016, MNRAS, 459, 3377 (R16)
Rybicki G. B., Lightman A. P., 1979, Radiative Processes in Astrophysics. Wiley-Interscience, New York
Safranek-Shrader C., Montgomery M. H., Milosavljević M., Bromm V., 2016, MNRAS, 455, 3288
Schleicher D. R. G., Palla F., Ferrara A., Galli D., Latif M., 2013, A&A, 558, A59
Shang C., Bryan G. L., Haiman Z., 2010, MNRAS, 402, 1249
Shibata M., Uchida H., Sekiguchi Y. i., 2016, ApJ, 818, 157
Shull J. M., van Steenberg M. E., 1985, ApJ, 298, 268
Stacy A., Greif T. H., Bromm V., 2010, MNRAS, 403, 45
Stecher T. P., Williams D. A., 1967, ApJ, 149, L29
Tanaka T. L., Li M., 2014, MNRAS, 439, 1092
Tseliakhovich D., Hirata C., 2010, Phys. Rev. D, 82, 083520
Turk M. J., Smith B. D., Oishi J. S., Skory S., Skillman S. W., Abel T., Norman M. L., 2011, ApJS, 192, 9
Valiante R., Schneider R., Volonteri M., Omukai K., 2016, MNRAS, 457, 3356
Verner D. A., Ferland G. J., Korista K. T., Yakovlev D. G., 1996, ApJ, 465, 487
Visbal E., Haiman Z., Bryan G. L., 2014a, MNRAS, 442, L100
Visbal E., Haiman Z., Bryan G. L., 2014b, MNRAS, 445, 1056
Wise J. H., Abel T., 2007, ApJ, 671, 1559
Wise J. H., Abel T., 2011, MNRAS, 414, 3458
Wise J. H., Cen R., 2009, ApJ, 693, 984
Wise J. H., Turk M. J., Abel T., 2008, ApJ, 682, 745
Wishart A. W., 1979, MNRAS, 187, 59P
Wu X. B. et al., 2015, Nature, 518, 512
Xu H., Wise J. H., Norman M. L., 2013, ApJ, 773, 83
Yoshida N., Abel T., Hernquist L., Sugiyama N., 2003, ApJ, 592, 645
Zdziarski A. A., Grove J. E., Poutanen J., Rao A. R., Vadawale S. V., 2001, ApJ, 554, L45

This paper has been typeset from a TEX/LATEX file prepared by the author.